



Technical Paper

Influence of helix bending deflection on the load transfer mechanism of screw piles in sand: Experimental and numerical investigations [☆]

Hung Manh Ho ^{a,*}, Adnan Anwar Malik ^b, Jiro Kuwano ^b, Hafiz Muhammad Awais Rashid ^c

^a Bentley Systems Singapore, Singapore; formerly at Saitama University, Japan

^b Graduate School of Science and Engineering, Saitama University, Japan

^c Department of Geological Engineering, University of Engineering and Technology Lahore, Pakistan; formerly at Saitama University, Japan

Received 15 October 2020; received in revised form 9 March 2021; accepted 2 April 2021

Abstract

This study investigates the load transfer mechanism that includes the effect of helix bending deflection on end-bearing capacity, distribution of ground pressure under the helix and soil deformation around the screw pile. The helix to shaft diameter ratio of 2.5 and 2.8 with a strong helix and a weak helix were used. The model ground was prepared with fine sand at 80% of relative density. To investigate the load transfer mechanism, the experimental tests were modelled in a 3D finite element code. A good agreement between the experimental and numerical approaches was found. The numerical analyses showed that large influence zone exists under screw pile with strong helix, which resulted in higher mobilized soil shear strength that contributed to higher end-bearing capacity. In the case of strong helix, uniform pattern of pressure distribution was observed under the central shaft and the helix. Similar pattern of pressure distribution under the central shaft was observed in weak helix case but the pattern of pressure distribution under the helix changed from uniform to triangular to trapezoidal at various stages during the load test. The normalized end-bearing capacity decreased linearly with the increase in normalized helix bending deflection in both approaches, i.e. experimental and numerical.

© 2021 Production and hosting by Elsevier B.V. on behalf of The Japanese Geotechnical Society. This is an open access article under the CC BY-NC-ND license (<http://creativecommons.org/licenses/by-nc-nd/4.0/>).

Keywords: Screw pile; Compressive load; Helix bending deflection; Load transfer mechanism; End-bearing capacity; Pressure distribution

1. Introduction

Screw piles are widely used because of their several advantages, such as easy installation, minimal required equipment, removability and reusability, minimum produced noise and vibration during installation and cost-effective (Livneh and El Naggar, 2008; Mohajerani et al., 2016). Furthermore, helical piles are installed mostly by the use of mechanical torque, which reduces the damage to adjacent structures, and can be constructed without excavation or pouring concrete (Livneh and El Naggar,

2008). The shape of the central shaft can be circular or square, and the helices can be fixed along the length of the shaft at specified distance (Li and Deng, 2019). In case of multiple helices with similar helix pitch, the installation becomes easy as each helix will follow same path (Mohajerani et al., 2016). Moreover, with the increase in the number of helices the ultimate resistance under compressive load also increases (Mittal and Mukherjee, 2015). According to Nagai et al. (2018), the load-settlement response depends upon installation method, however, if the load on the pile tip reached second-limit uplift resistance then the installation method has no effect.

The design of screw pile is generally based on cylindrical shear method and individual bearing method. In cylindrical shear method the total compressive resistance of the screw

Peer review under responsibility of The Japanese Geotechnical Society.

* Corresponding author.

E-mail address: hung.homanh@bentley.com (H.M. Ho).

<https://doi.org/10.1016/j.sandf.2021.04.001>

0038-0806/© 2021 Production and hosting by Elsevier B.V. on behalf of The Japanese Geotechnical Society.

This is an open access article under the CC BY-NC-ND license (<http://creativecommons.org/licenses/by-nc-nd/4.0/>).

pile consisted of end-bearing below the bottom helix, cylindrical shear resistance along the helices and shaft resistance above the top helix (Livneh and El Naggar, 2008; Sakr, 2011, 2009). In individual bearing method the total compressive resistance of the screw pile consisted of end-bearing at each helix and shaft resistance (Livneh and El Naggar, 2008; Sakr, 2011, 2009). The axial capacity of screw pile can be correlated with the torque factor which depends upon the type of soil, the geometry of pile, mechanical properties of soil, loading direction and installation depth (Ghaly and Hanna, 1991; Sakr, 2014; Tsuha and Aoki, 2010). The lateral resistance of screw pile increases with the increase in number of helices up to certain depth, after that it increases moderately (Mittal et al., 2010). According to Lanyi-Bennett and Deng (2019), under group pile, individual bearing failure exists.

The screw pile performance not only depends upon the geotechnical aspects of the ground but also on the structural aspects of the pile which ultimately affect the geotechnical performance of the screw pile. Previous studies have shown that helix bending deflection affects pile resistance (Malik et al., 2019; Malik and Kuwano, 2020; Yttrup and Abramsson, 2003), however, the load transfer mechanism was not studied clearly. In this study, numerical analysis results are validated with experimental results to investigate the load transfer mechanism that includes the effect of helix bending deflection on end-bearing capacity, distribution of ground pressure under the helix at various stages of loading, and soil deformation around the screw pile.

In order to achieve the above-stated objectives, closed-end screw piles were used. The model ground was prepared in dense state. Experiments were carried out and numerical analysis of the experimental models were performed to get an insight view of the load transfer mechanism of the screw piles with both strong and weak helices under vertical loads in dense sand. The strong helix is considered as the one which do not deform during the test, and the weak helix is considered as the one which deforms during the test. Model screw piles having helix diameter of 55 and 60 mm with helix thickness of 0.8 and 3.0 mm were used

in this study. The helix to shaft diameter ratio of the model pile was 2.5 - 2.8.

2. Experimental modelling

2.1. Experimental set up

Dry Toyoura sand with a relative density (D_r) of approximately 80% was used for the ground model. The sand was prepared in each layer of 100 mm in thickness to get the derived relative density. The properties of Toyoura sand are as follows: Specific gravity = 2.645; $D_{50} = 0.20$ mm; $e_{min} = 0.609$; $e_{max} = 0.973$.

The closed-end model screw pile with a single helix was used in this study (Fig. 1a). The material of the pile shaft and helix was STK400 and SS400 with Young's modulus of 2.11×10^8 kN/m², yield strength of 2.35×10^5 kN/m², tensile strength of 4×10^5 kN/m² and Poisson's ratio of 0.293. To only examine the effect of helix bending deflection on the bearing performance, the pile installation was not considered, and the helix was modeled as a flat circular plate, as shown in Fig. 1. According to Mori (2003), the intersection angle of toe wing does not affect the toe resistance per unit area. A slit of 5 mm was provided on the helix to simulate the actual condition of the helix, i.e. not a complete circle (Fig. 1b). The strain gauges were attached at the top of the pile and above the helix to measure the friction resistance along the shaft. The screw pile length (L) of 500 mm and shaft diameter (D_s) of 21.7 mm were used for all pile tests.

The pile was set up in a cylindrical steel container with inner diameter of 592 mm and depth of 700 mm (Fig. 1c). The thickness of the bottom and side wall of the container was 25.5 mm and 9 mm, respectively. Therefore, the model container was considered as a rigid body. The previous studies suggested that the zone in which soil is affected by loading is usually 3–8 times of the pile tip diameter (Kishida, 1963; Robinsky and Morrison, 1964). Yang (2006) proposed that the influence zone in clean sand above and below the pile tip should be $1.5D$ – $2.5D$ and $3.5D$ – $5.5D$, respectively, where D is the pile diameter. In

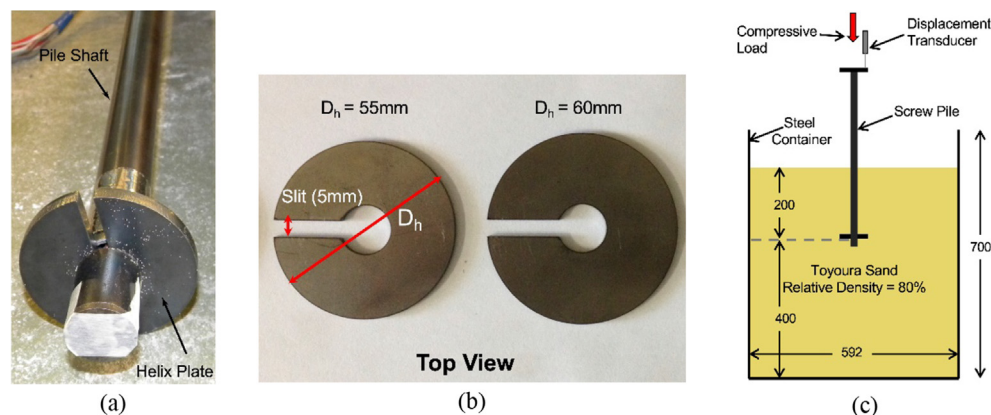


Fig. 1. (a) Screw pile model and strain gauge positions (b) helices models (c) model container, units in mm.

this study, the clearance around the pile was 9.9–10.8 times the pile diameter and the clearance below the pile was 400 mm (6.7–7.2 times pile tip diameter). Therefore, the effect of the boundary condition is ignored.

The ratio of the helix diameter to shaft diameter, D_h/D_s , is commonly 2 to 4 in practice (Elsherbiny and El Nagggar, 2013; Sakr, 2009; Yttrup and Abramsson, 2003). The helix plates having diameter of 55 and 60 mm (D_h/D_s , 2.5 - 2.8) were used. In order to investigate the effect of helix bending deflection on the ground, both strong and weak helices were used. The strong helix with thickness of 3.0 mm represents the non-deformed scenario (negligibly small deflection that does not affect the load-settlement response) whereas, weak helix with thickness of 0.8 mm represents deformed scenario (the helix bending deflection affects the load-settlement response). The experimental tests cases which are considered in this study are shown in Table 1.

2.2. Testing procedures

The dry Toyoura sand was compacted in six layers with the thickness of each layer of 100 mm. The relative density of each layer was approximately 80% (unit weight of 15.42 kN/m³). After preparing four sand layers, the screw pile was placed, and then the upper two layers of 100 mm were compacted. This procedure was adopted to exclude the effect of the pile installation on the model ground. The settlement (U) of the screw pile was measured at the head through a displacement transducer, and the applied compressive load (P) was measured by a load cell. To investigate the effect of helix bending deflection on the end-bearing capacity, the ground conditions were kept similar for all tests.

3. Numerical modelling

3.1. Material models

The main objective of the numerical models is to get an insight view of the load transfer mechanism of the screw pile under vertical loads. The finite element model (FEM) provided the effects of pile loading on the surrounding soil and pressure beneath the helices.

Linear elastic model was used for the pile shaft. The strong helix experimental cases, i.e. Case 1_Exp and Case 3_Exp with helix thickness of 3.0 mm were modeled exactly in the numerical model. Whereas, the weak helix experi-

mental cases, i.e. Case 2_Exp and Case 4_Exp with helix thickness of 0.8 mm were modeled with helix thickness of 3.0 mm but the stiffness (EI) of the helix was reduced by a factor to get the similar helix bending deflection as in the experiment. The reason for not modeling the thin helix thickness of 0.8 mm was due to poor mesh quality it created, which resulted in calculation convergence and accuracy issues.

The ground was modelled using the Hardening soil model with small-strain stiffness (HSS model) (Benz, 2007). This model is extended for small strain range from the original Hardening soil (HS) model (Schanz et al., 1999), which takes into account for stress and strain-dependent stiffness, and it is based on the hyperbolic stress-strain relationship between the axial strain, ϵ_1 and the deviatoric stress, q shown in Fig. 2. The HS and HSS models have been used successfully for back analyses of projects (Broere and Van Tol, 2006; Calvello and Finno, 2004; Finno and Calvello, 2005; Hejazi et al., 2008; Likitlersuang et al., 2013; Suryasentana and Lehane, 2014; Unsever et al., 2015), therefore, it was selected for the ground modelling.

The stress-strain behavior under primary loading is non-linear and is assumed to be hyperbolic up to a failure stress shown in Fig. 2 for the HS and HSS models. The extension for the small-strain stiffness is illustrated in Fig. 3. The maximum stress is determined based on the Mohr-Coulomb failure criteria involving strength parameters, c' and ϕ' . Stiffness E_{50} is used to determine both elastic and plastic strains, E_{ur} is an elasticity modulus. Both the secant primary loading modulus E_{50} and unloading/reloading modulus E_{ur} are stress-dependent and indicated below:

$$E_{50} = E_{50}^{ref} \left(\frac{c' \cos \phi' - \sigma_3' \sin \phi'}{c' \cos \phi' + p^{ref} \sin \phi'} \right)^m \quad (1)$$

$$E_{ur} = E_{ur}^{ref} \left(\frac{c' \cos \phi' - \sigma_3' \sin \phi'}{c' \cos \phi' + p^{ref} \sin \phi'} \right)^m \quad (2)$$

where E_{50}^{ref} and E_{ur}^{ref} are input parameters for a particular reference pressure p^{ref} . The exponent m can be measured in both oedometer tests and in triaxial tests.

Another stiffness is the oedometer modulus (E_{oed}^{ref}), and it is used to control the magnitude of the plastic volume strains. In a similar manner to the triaxial moduli, the oedometer stiffness also follows a stress dependency according to the formula:

Table 1
Experimental cases.

Cases	Pile shaft length, L (mm)	Helix diameter, D_h (mm)	D_h/D_s	Helix thickness, T_h (mm)	Remarks
Case 1_Exp	500	55	2.5	3.0	21.7-55-3_Exp
Case 2_Exp	500	55	2.5	0.8	21.7-55-0.8_Exp
Case 3_Exp	500	60	2.8	3.0	21.7-60-3_Exp*
Case 4_Exp	500	60	2.8	0.8	21.7-60-0.8_Exp

* 21.7-60-3_Exp: Shaft Diameter-Helix Diameter-Helix thickness_Experiment.

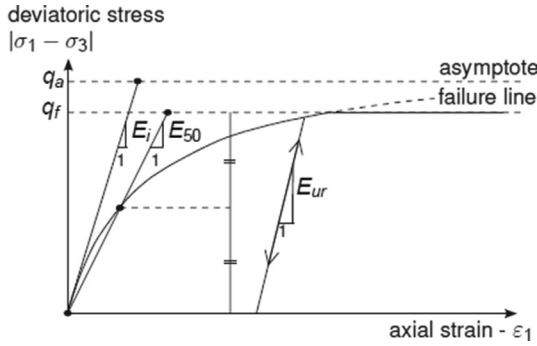


Fig. 2. Hyperbolic stress-strain relation of HS model (Schanz et al., 1999).

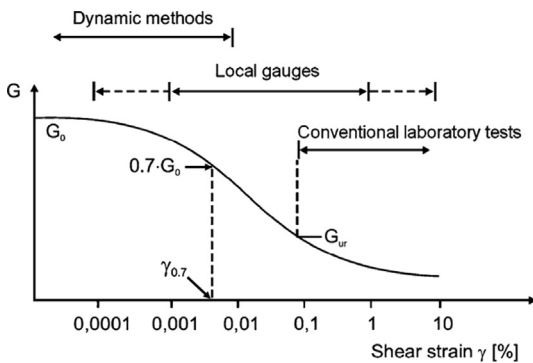


Fig. 3. Small-strain stiffness curve of HSS (Benz, 2007).

$$E_{oed} = E_{oed}^{ref} \left(\frac{c' \cos \phi' - \sigma'_1 \sin \phi'}{c' \cos \phi' + p^{ref} \sin \phi'} \right)^m \quad (3)$$

where E_{oed}^{ref} is an input parameter. It is noted that the reference triaxial stiffness is obtained by normalizing to the minor principal stress, σ'_3 , and the reference oedometer stiffness by normalizing to the major principal stress, σ'_1 , in an oedometer test.

The tangent shear modulus at small strains can be formulated as follows:

$$G_t = \frac{G_0}{\left(1 + 0.385 \frac{\gamma}{\gamma_{0.7}}\right)^2} \quad (4)$$

where G_0 is the initial or very small strain shear modulus and $\gamma_{0.7}$ is the shear strain level at which the secant shear modulus G_s is reduced to 70% of G_0

The input soil parameters in this study were determined based on the back calculation of a test result with the same sand and relative density presented by Nakai and Hinokio (2004), which is shown in Fig. 4. The determined soil properties are shown in Table 2. This internal friction angle of the Toyoura sand in the HSS model is close to its value of 40° in the triaxial consolidated drained shear (CD) tests with the same relative density (80%) presented by Matsumoto et al. (2010).

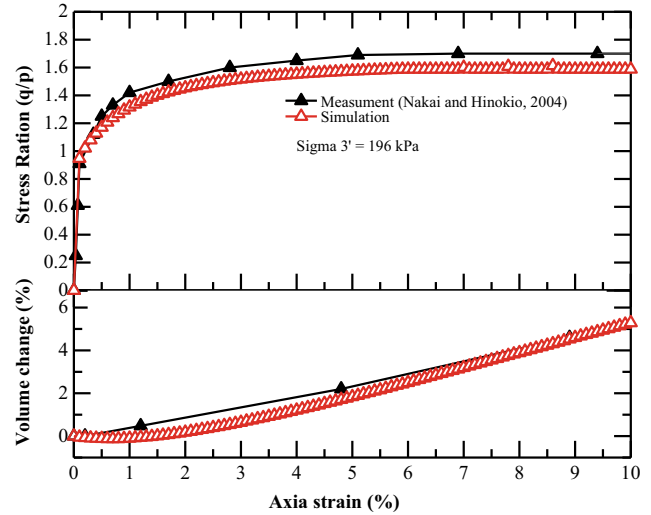


Fig. 4. Stress ratio (q/p) and Volume strain vs Axial strain of triaxial compression test ($\sigma'_3 = 196$ kPa).

Table 2
Material properties of Toyoura sand.

Items	Values
Secant stiffness E_{50}^{ref} (kPa) ^a	29,000
One-dimensional, E_{oed}^{ref} (kPa) ^a	30,000
Unloading stiffness, E_{ur}^{ref} (kPa) ^a	85,000
Stress dependency parameters, m	0.5
Failure ratio q_f/q_a , R_f	0.9
Poisson's ratio, ν_{ur}	0.2
Internal friction angle, $\phi'(^{\circ})$	38.79
Dilatancy angle, $\psi(^{\circ})$	15
Threshold shear strain, $\gamma_{0.7}$	0.25E-3
Shear modulus at small strain, G_0^{ref}	260,000

^a value for a reference stress, $p_{ref} = 100$ kPa.

3.2. Numerical modelling of experiments

Three-dimensional models were created using a finite element code, PLAXIS 3D (Bentley, 2020) for the simulation of the experimental tests. The finite element mesh of the model having pile with helix diameter of 60 mm is shown in Fig. 5. A half model was simulated due to the symmetric configuration, which helped the model to reduce the number of elements, and the mesh could be refined to get better results. The mesh around the pile was finer (refined) than other soil clusters to get accurate results.

Potyondy (1961) showed that the soil-structure interaction depends on soil grading, density, stress level, interface material and surface roughness. Usesugi and Kishida (1986) pointed out that the maximum coefficient of friction between Toyoura sand and mild steel, $\tan \delta/\phi$, were 0.6 and 0.87 for the density of 45% and 90%, respectively. In this study, $\tan \delta/\phi$, is taken to be 0.85. The HSS model was used to model the ground condition for all models. The interaction between the pile and ground was simulated

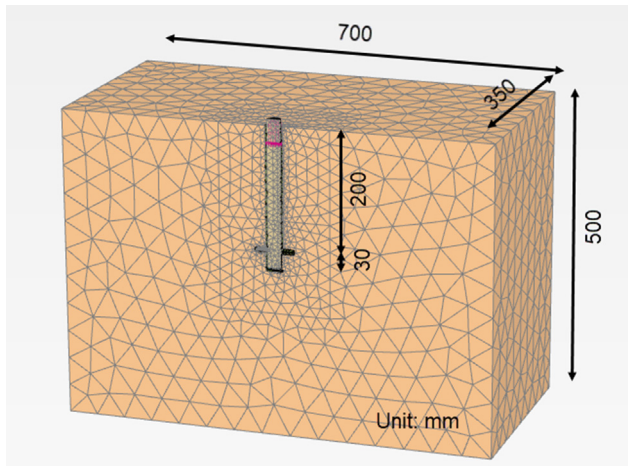


Fig. 5. Finite element mesh of Screw pile.

with the interface element, which is modelled based on the Elastic perfectly plastic model.

The screw pile resistance also depends on the helix bending deflection (Malik et al., 2019); therefore, in this study, the helix was assumed to behave elastically. The helix thickness was 3.0 mm, and it was not changed for all numerical cases. For thinner helix (weak helix) thickness (<3 mm), its bending stiffness (EI) was reduced by reducing Young's modulus, E , to get the similar helix deflection (y) as in the experimental results. Twelve cases with different stiffness (EI) are shown in Table 3. The numerical cases, Case 1_Num and Case 7_Num were representing the experimental cases, Case 1_Exp and Case 3_Exp in which helix thickness (3.0 mm) and its bending stiffness (EI) were identical. In addition, the numerical cases, Case 6_Num and Case 12_Num were representing the experimental cases Case 2_Exp and Case 4_Exp in which helix thickness of 3.0 mm was considered but its bending stiffness was reduced to get the similar bending deflection of helix as in experimental case. Other numerical models with different stiffness were simulated to get the relationship between the helix bending deflection and its end-bearing pile capacity.

Table 3
Numerical modelling cases.

Cases	Helix diameter (D_h) (mm)	D_h/D_s	Bending Stiffness (EI)	Remarks	
Case 1_Num	55	2.5	EI	Same as Case 1_Exp	21.7-55-3_Num
Case 2_Num	55	2.5	$EI/25$		
Case 3_Num	55	2.5	$EI/100$		
Case 4_Num	55	2.5	$EI/150$		
Case 5_Num	55	2.5	$EI/250$		
Case 6_Num	55	2.5	$EI/550$	Same as in Case 2_Exp	21.7-55-0.8_Num
Case 7_Num	60	2.8	EI	Same as in Case 3_Exp	21.7-60-3_Num*
Case 8_Num	60	2.8	$EI/25$		
Case 9_Num	60	2.8	$EI/50$		
Case 10_Num	60	2.8	$EI/100$		
Case 11_Num	60	2.8	$EI/150$		
Case 12_Num	60	2.8	$EI/250$	Same as in Case 4_Exp	21.7-60-0.8_Num

$E = 2.11 \times 10^8$ kN/m².

* 21.7-60-3_Num: Shaft Diameter-Helix Diameter-Helix Thickness_Numerical modelling.

4. Results and discussions

4.1. Load-settlement response

The failure criteria for bearing capacity of pile is estimated at 10% diameter of piles (BS 8004, 2004; ISSMFE, 1985; Yttrup and Abramsson, 2003). Livneh and El Naggar (2008) proposed the critical failure is 8% of the diameter of the largest helix plus the elastic settlement of the pile. Therefore, in this study, the head settlement of 10% helix diameter, i.e. 5.5 mm and 6.0 mm, was accepted for the failure criteria for the screw piles with $D_h = 55$ mm and 60 mm, respectively. The pile behavior at this settlement (10% D_h) is mainly used for the analyses.

The axial force along the piles from the top until just above the helices in the experimental results are shown in Fig. 6. The axial forces at the pile top are 3.9/ 2.8 kN for the piles 21.7-55-3/0.8 at the pile head settlement, $y = 5.5$ mm (10% D_h), and 4.4/ 3.2 kN for the piles 21.7-60-3/0.8 at $y = 6.0$ mm, respectively. The friction along the pile is very small for all piles, i.e. 0.07/0.15 kN for the pile 21.7-55-3/0.8 and 0.09/0.13 kN for the pile 21.7-60-3/0.8, respectively. This means that the skin friction is negligible and almost all applied compressive load transferred to the end-bearing component. The finite element results also shows the similar axial force distribution, which is quite uniform along the piles. However, the skin resistance accounted for a larger proportion compared to it in the experimental test, i.e. around 10% for the piles with the strong helices and 15% for the pile with the weak helices. In general, a good agreement between experimental and numerical results are found. In numerical analysis, the axial force observed at a depth of 5 cm was slightly smaller than the axial force at 10 cm (for all piles), which is not physically logical. The reason could be that this extracted force was calculated by integrating the pile stresses on its area of a cross-section (at 5 cm depth). The stresses on the section were interpolated from stress points (Gauss points), which were used for the calculation in the program (PLAXIS manual). This means that those stresses on a sec-

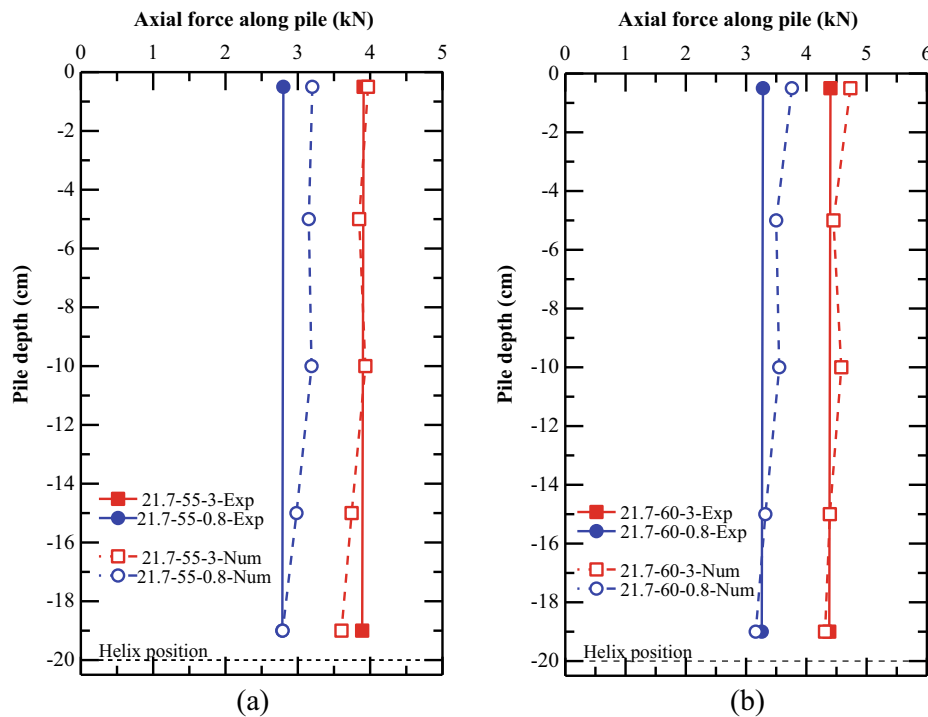


Fig. 6. Axial force along piles at pile head settlement of (a) 5.5 mm for $D_h = 55$ mm, (b) 6.0 mm for $D_h = 60$ mm.

tion were not so much accurate (note that stress points were used for the calculation). Stresses on a section were mainly used for visualization and post-process. Furthermore, the force at a depth of 5 cm is also slightly smaller than the force at pile top, which was consistent with the applied load. So, it can be acceptable.

Fig. 7 shows the load-settlement curves obtained from experiments and numerical analyses and helix deformation after the experiments. Again, a good match is obtained in experimental and numerical load-settlement curves for both cases, i.e. strong helix (Case 1_Exp/Num and Case 3_Exp/Case 7_Num) and weak helix (Case 2_Exp/Case 6_Num and Case 4_Exp/Case 12_Num). However, in case of weak helix, the difference between experimental curve and numerical analysis curve is more after pile settlement of 4 mm, but after point A the difference becomes less as the penetration resistance increases in experimental results as shown in Fig. 7(a, b). The increase in penetration resistance after point A is presumed to be due to the strain hardening in the helix due to large bending deformation (at large deflection circular plate shows re-stiffening (Winter and Levine, 1978), which restrict further bending of helix). Hence, after point A only ground deformation exists, which provides increase in penetration resistance. This behavior is not observed in the numerical analysis, as the helix is modelled as the linear elastic model. However, at the plunging resistance state (the ultimate state of the ground at which the pile settlement increases without further increase in vertical load or constant loading rate), experimental and numerical curves are very close to each other. As illustrated in Fig. 7a and 7b, in the experimental results, the end-bearing capacity (measured

at settlement equals of 10% of D_h) of screw pile is reduced around 23% due to helix bending deflection, and it is quite similar to the numerical results in which the reduction is around 21%.

4.2. Load transfer mechanism

As the experimental observations could not provide the interaction between the pile and surrounding soil, the finite element analyses are utilized, which provided insight views of pressure distribution beneath helices and deformation of the surrounding soil. In order to utilize the finite element results for understanding the load transfer mechanism, the boundary stresses measured in the simulation model should be comparable with the boundary stresses in the experimental model. The stresses on the container boundary (on the container's wall and floor) were measured through pressure transducers during the pile load test. These measured stresses were comparable with the stresses measured at the boundary in the numerical simulation. Therefore, the soil's stress conditions obtained from numerical simulation can be considered the soil's stress conditions in a small-scale model test. The finite element results of the helix diameter of 60 mm are analyzed at the settlement of 10% D_h ($U_z = 6.0$ mm) and presented in details below.

Soil displacement is commonly used to estimate an influence zone and the failure surface (Yamamoto and Kusuda, 2001). The soil total displacement shadings of 10% increment are shown in Fig. 8. As illustrated, in case of strong helix the influence zone (where soil displacements are

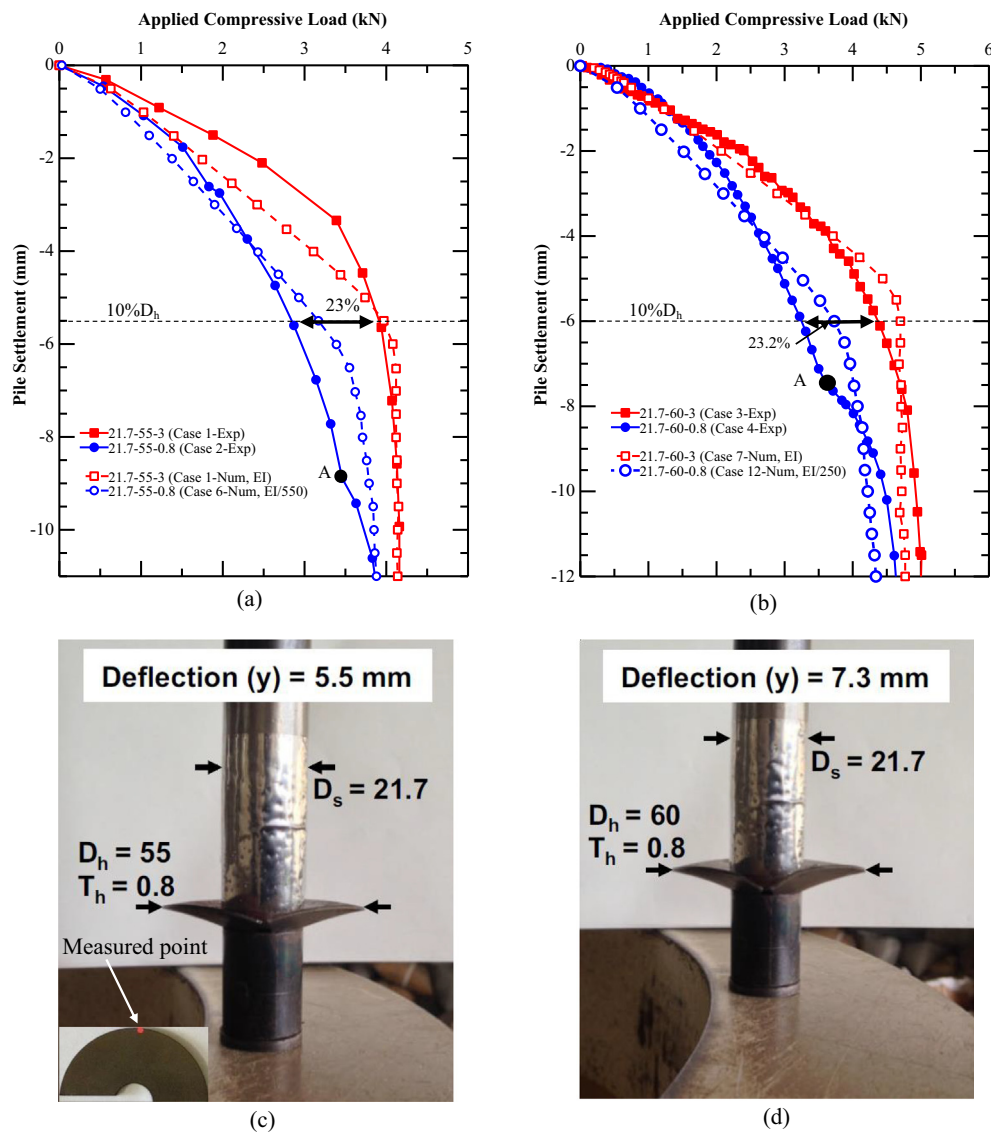


Fig. 7. Load-settlement curves (a) Helix diameter, D_h , = 55 mm (b) D_h = 60 mm (c) deformed helix after pile test of D_h = 55 mm (Malik et al., 2019) (d) D_h = 60 mm (Malik et al., 2019).

greater than 20% of the total soil displacement) ranged $2.7D_h$ above, $1.8D_h$ below the helix and $1.9D_h$ in the horizontal direction. While in the case of a weak helix, the influence zone ranged $2.3D_h$ above, $1.5D_h$ below the helix and $1.5D_h$ in the horizontal direction. The observed influence zone of strong helix in this study is quite consistent with the study of Livneh and El Naggar (2008). Moreover, in case of the strong helix, the large soil displacement is observed below the whole helix. While, in case of the weak helix, it is observed close to the shaft.

The influence zone is large in strong helix (Fig. 8) case, therefore, the mobilized soil shear strength (the maximum shear stress, greater than 100 kPa) zone is also large (Fig. 9) which resulted in a higher bearing capacity, and it is clearly observed in load-settlement curves (refer Fig. 7a, b). The large mobilized shear strength is observed below the helix, which reflected the contribution of

end-bearing. In case of strong helix, the mobilized shear strength combinedly developed under the central shaft and helix. Whereas, in case of weak helix, the mobilized shear strength separately developed under the central shaft and helix as shown in Fig. 9. It is also observed that the mobilized shear strength generated above the helix, i.e. outside the influence zone. However, its value is smaller than 100 kPa and it is not visible in Fig. 9.

The pressure on the helix's upper face is minimal compared to the pressure under the helix because the soil in this zone is dilated when the pile is penetrated down. This means that the pressure under the helix mainly affects the pile behavior. Moreover, the end-bearing capacity of screw pile under strong helix and weak helix is closely related to the pressure distribution under the helix. In this study, this pressure distribution is investigated through the finite element analyses at three location on the load-settlement

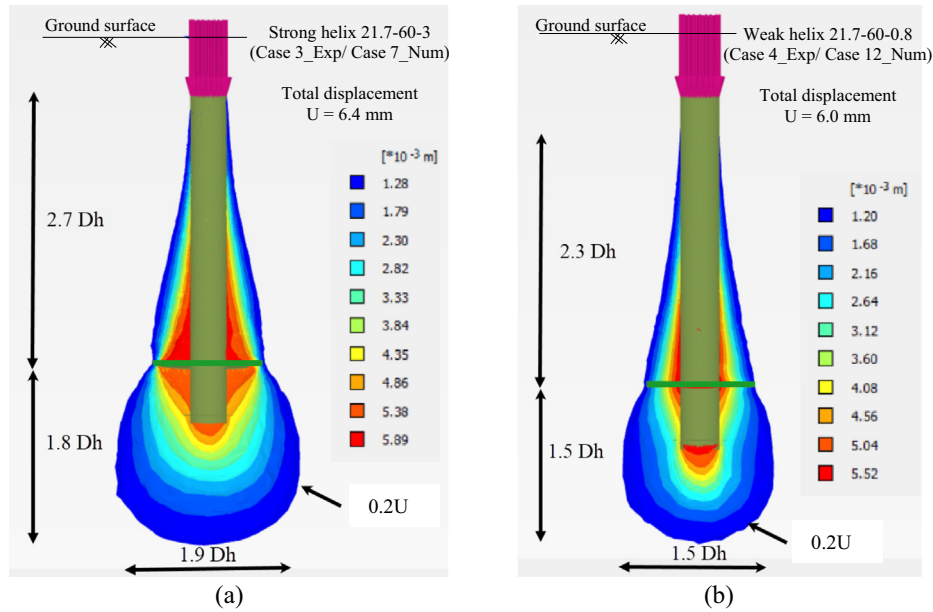


Fig. 8. Total soil displacement (a) for strong helix (b) for weak helix.

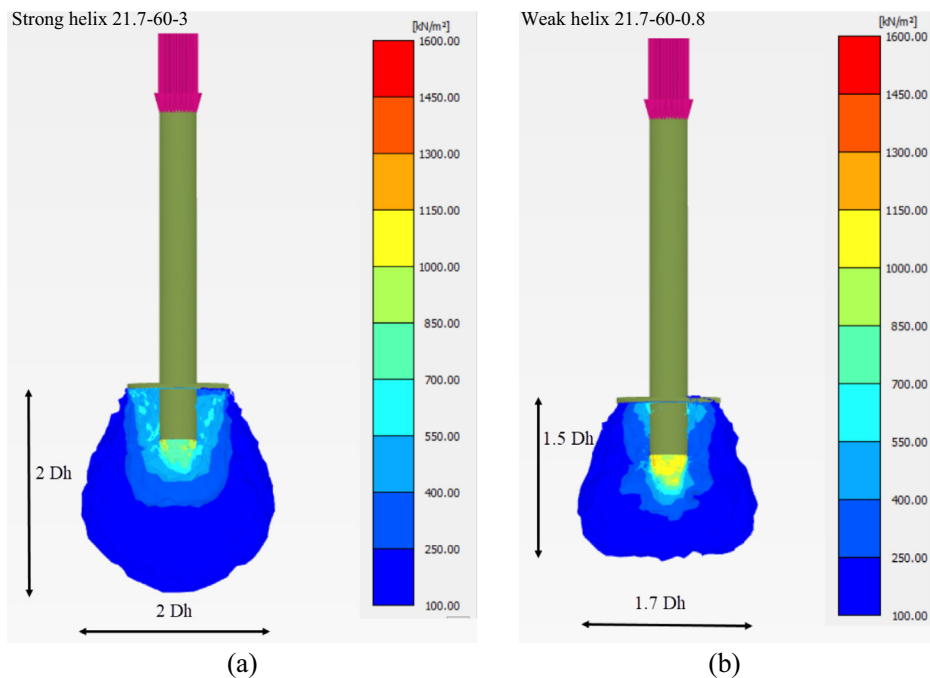


Fig. 9. Mobilized soil shear strength (a) for strong helix (b) for weak helix.

curve, i.e. Initial stage: at settlement of 0.5 mm, Transition stage: at 10% of D_h , Plunging resistance stage: at 20% of D_h . The initial stage represents the situation in which the helix bending deflection does not affect the load settlement response (critical helix bending deflection, 0.41–0.81 mm (Malik et al., 2019): 0.5 mm considered). The transition stage represents the situation in which the ground is in transition nonlinear region (considered at 10% of D_h). Whereas, the plunging resistance stage represents the situation in which the ground in final linear region, i.e. the ultimate

state of the ground at which the pile settlement increases without further increase in vertical load or pile settlement increases at constant loading rate (considered at 20% of D_h).

The results of finite element analyses indicated that the pressure distribution under the strong and weak helix are identical at the initial stage of the load-settlement curve, as shown in Fig. 10(a, b). Moreover, the pressure under the central shaft (350 kPa) is 2.05 times the pressure under the helix (170 kPa), which is very close to the previous

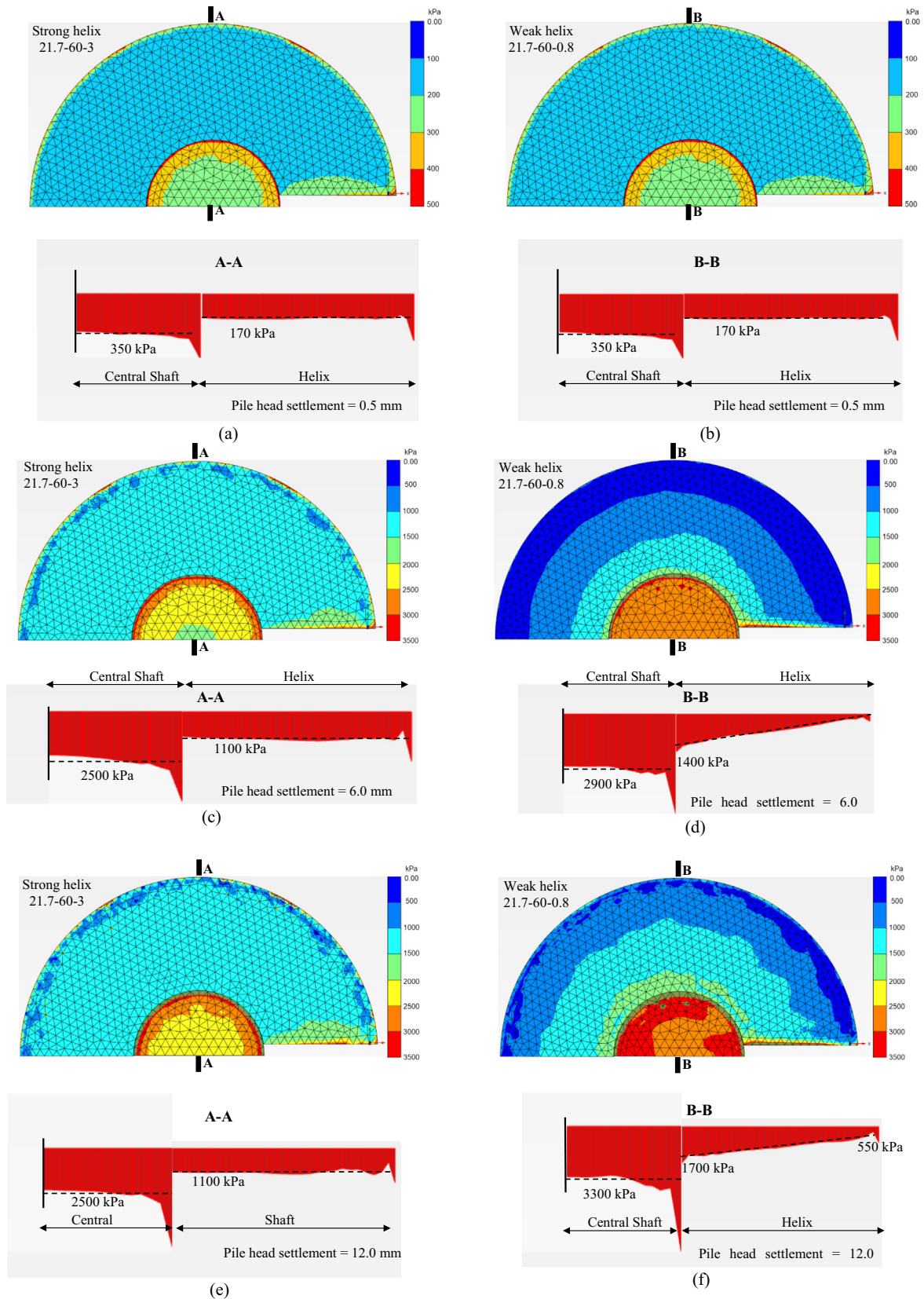


Fig. 10. Pressure distribution under the screw pile (a) Strong helix: Initial stage (b) Weak helix: Initial stage (c) Strong helix: Transition stage (d) Weak helix: Transition stage (e) Strong helix: Plunging resistance stage (f) Weak helix: Plunging resistance stage.

study (Yttrup and Abramsson, 2003) for strong helix case. As the helix bending deflection is very small (in weak helix case) and it does not affect the ground condition, that is why at the initial stage the pressure distribution for strong and weak helix are same. Uniform pattern of pressure distribution is observed under the central shaft and the helix for both screw piles, i.e. strong and weak helix screw piles.

At transition stage (at settlement equals to 10% of D_h), the results indicated that the pressure distribution under the strong and weak helix are not similar as shown in Fig. 10 (c, d). In the case of strong helix, the pressure distribution is similar to the initial stage, i.e. uniform pattern of pressure distribution under the central shaft (2500 kPa) and helix (1100 kPa) but the pressure distribution ratio (central shaft/helix) increased from 2.05 to 2.27. In the case of weak helix, the pattern of pressure distribution under the central shaft remains the same, i.e. uniform pressure distribution but under the helix, the pressure distribution changed from uniform to triangular pattern as shown in Fig. 10 (b, d). The maximum pressure (1400 kPa) under the helix is observed near the central shaft which reduced linearly and approached to zero at the outer edge of the helix as shown in Fig. 10d. This reduction in pressure under the helix is due to the bending of helix during loading which resulted in lesser soil resistance below the helix (refer Fig. 9b). Uniform pressure distribution (2900 kPa) is observed under the central shaft, and this pressure distribution is 2.07 times the pressure on the inner edge of the helix (1400 kPa, near the central shaft). At transition stage, the pressure under the central shaft is more in weak helix pile than the strong helix pile, i.e. 2900 kPa compared to 2500 kPa. This is due to the smaller helix's relative stiffness than the central shaft, especially when it deforms, which resulted in more load transfer from the helix to the central shaft.

At plunging resistance stage (ultimate state of the ground), the results indicated that the pressure distributions under the strong and weak helices are also not similar as shown in Fig. 10 (e, f). In the case of strong helix, the pressure distribution is similar to the initial and transition stages, i.e. uniform pattern of pressure distribution under the central shaft (2500 kPa) and helix (1100 kPa). The pressure distribution ratio (central shaft/helix) is similar to the transition stage, i.e. 2.27. In case of weak helix, the pattern of pressure distribution under the central shaft is similar to initial and transition stage, i.e. uniform pressure distribution but under the helix the pressure distribution changed from triangular pattern to trapezoidal pattern as shown in Fig. 10 (d, f). The maximum pressure (1700 kPa) under the helix is observed near the central shaft which reduced linearly and approached to 550 kPa at the outer edge of the helix as shown in Fig. 10f. The non-zero pressure at the outer edge of the helix is due to large deformation of the soil with respect to helix bending deflection. As the helix bending deflection is less, therefore, the whole pile moved downward, resulting in redistribution of pressure at the outer part of the helix. In this stage as well, the pres-

sure under the central shaft is more in weak helix pile than the strong helix pile.

The average pressure under the central shaft and helices with different helix stiffness (EI , representing the change in helix thickness) at transition stage (at settlement equals to 10% of D_h) is shown in Fig. 11. The finite element analysis results indicate the pressure under the central shaft and at the inner edge of the helix increased with the decrease in helix stiffness, i.e. from 2500 to 2900 kN/m² and 1100 to 1400 kN/m², respectively. However, at the outer edge of the helix the pressure decreased with the decrease in helix stiffness, i.e. 1100 kN/m² to zero as shown in Fig. 11. The reason for this change in pressure distribution under the central shaft and helix is due to the helix bending deflection during the applied load. As the helix deformed, relative displacement between the soil beneath helix and central shaft occurred, the helix's relative stiffness was smaller than that of the central shaft. Therefore, more load transferred to the central shaft and the pressure shifted from the outer edge of the helix to the central shaft.

4.3. Helix bending deflection and end-bearing bearing capacity

Malik et al. (2019) showed that the reduction of end-bearing resistance due to the helix bending deflection (y) was more in a screw pile with larger helix diameter (D_h). Therefore, the helix bending deflection should be normalized by the helix diameter, $y/[(D_h - D_s)/2]$. The relationship between the helix bending deflection and end-bearing capacity (P_u) is presented based on the ratio of $y/[(D_h - D_s)/2]$ versus P_u/P_{u-max} . Where P_{u-max} is the maximum capacity of the ground obtained in non-deformed helix case (strong helix). The helix bending deflection in the experimental tests was measured after finishing the tests, and ultimate capacity of the ground was measured at plunging resistance stage (at settlement equals to 20% of D_h). The normalized helix bending deflection and end-bearing capacity of twelve numerical cases (strong to weak helix) and all experiments are plotted and shown in Fig. 12. A good agreement between experimental and numerical results is observed for the weak and strong helices. It

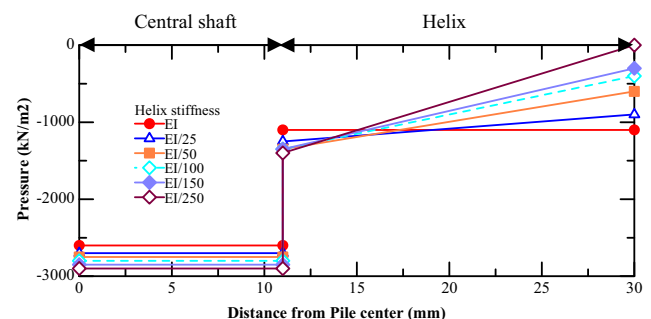


Fig. 11. Stresses under the central shaft and helices at varying helix stiffness (EI) for Case 7_Num to Case 12_Num.

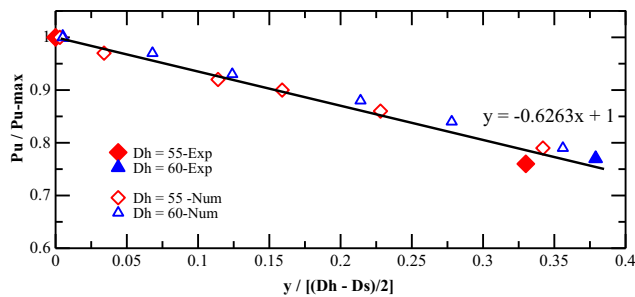


Fig. 12. The relationship between normalized helix bending deflection vs normalized end-bearing capacity.

clearly depicts that the normalized end-bearing capacity decreased linearly with the increase in normalized helix bending deflection.

5. Conclusions

This paper investigated the load transfer mechanism that includes the effect of helix bending deflection on end-bearing capacity, distribution of ground pressure under helix and soil deformation around the pile for single helix screw pile under dense ground condition. Two scenarios, i.e. strong helix (non-deformed helix) and weak helix (deformed helix) were considered through experimental and numerical analyses (PLAXIS 3D) to examine the load transfer mechanism. The results showed good agreement between experimental and numerical analyses for both strong and weak helices. Based on the analyses, the following conclusion are drawn:

In the case of strong helix, the influence zone ranged $2.7D_h$ above, $1.8D_h$ below the helix and $1.9D_h$ in the horizontal direction. While in the case of a weak helix, the influence zone ranged $2.3D_h$ above, $1.5D_h$ below the helix and $1.5D_h$ in the horizontal direction. This reduction in influence zone is due to the helix bending deflection. The large influence zone in strong helix case, resulted in higher mobilized soil shear strength (the maximum shear stress) which contributed to a higher end-bearing capacity of about 23% compared to the weak helix case.

Under the strong helix case, the pattern of pressure distribution, i.e. under the central shaft and helix, was uniform and remained the same throughout the load-settlement curve instead of highest near the shaft and lowest at the outer edge of the helix as suggested in previous studies. Moreover, the pressure under the helix is approximately half of that under the central shaft. Whereas in the weak helix case, the pressure distribution did not follow a single pressure pattern as indicated in previous studies, but it changed at different stages of the load-settlement curve. Under the helix (weak helix case), the pattern of pressure distribution changed from uniform (at initial stage of the load-settlement curve) to triangular (at transition stage of the load-settlement curve), and finally changed to trapezoidal (at plunging resistance stage of the

load-settlement curve). However, under the central shaft, the pattern of pressure distribution remained almost uniform throughout the load-settlement curve, but the magnitude of pressure was more than the strong helix case.

The numerical analysis indicated that the pressure under the central shaft and at the inner edge of the helix increased with the decrease in helix stiffness. However, at the outer edge of the helix the pressure decreased with the decrease in helix stiffness. The reason for this change in pressure distribution under the central shaft and helix was due to the helix bending deflection during the applied load, and it shifted the pressure from the outer edge of the helix to the central shaft.

The normalized end-bearing pile capacity (P_u/P_{u-max}) decreased linearly with normalized helix bending deflection $y/[(D_h - D_s)/2]$.

References

- Bentley, 2020. User Manual PLAXIS 3D. The Netherlands.
- Benz, T., 2007. Small-Strain Stiffness of Soils and its Numerical Consequences PhD thesis. University of Stuttgart.
- Broere, W., Van Tol, A.F., 2006. Modelling the bearing capacity of displacement piles in sand. Proc. Inst. Civ. Eng. Geotech. Eng. 159, 195–206. <https://doi.org/10.1680/jeng.2006.159.3.195>.
- BS 8004, 2004. British standard code of practice for foundations. Br. Standards Institution (BSI). London.
- Calvello, M., Finno, R.J., 2004. Selecting parameters to optimize in model calibration by inverse analysis. Comput. Geotech. 31, 410–424. <https://doi.org/10.1016/j.compgeo.2004.03.004>.
- Elsherbiny, Z.H., El Naggar, M.H., 2013. Axial compressive capacity of helical piles from field tests and numerical study. Can. Geotech. J. 50, 1191–1203. <https://doi.org/10.1139/cgj-2012-0487>.
- Finno, R.J., Calvello, M., 2005. Supported excavations: Observational method and inverse modeling. J. Geotech. Geoenviron. Eng. 131, 826–836. [https://doi.org/10.1061/\(ASCE\)1090-0241\(2005\)131:7\(826\)](https://doi.org/10.1061/(ASCE)1090-0241(2005)131:7(826)).
- Ghaly, La., Hanna, A.H.M., 1991. Installation torque of screw anchors in dry sand. Soils Found. 31, 77–92.
- Hejazi, Y., Dias, D., Kastner, R., 2008. Impact of constitutive models on the numerical analysis of underground constructions. Acta Geotech. 3, 251–258. <https://doi.org/10.1007/s11440-008-0056-1>.
- ISSMFE, 1985. Axial pile loading test - Part I: Static loading. ASTM 8, 79–80.
- Kishida, H., 1963. Stress distribution by model piles in sand. Soils Found. 4, 1–23.
- Lanyi-Bennett, S.A., Deng, L., 2019. Axial load testing of helical pile groups in glaciolacustrine clay. Can. Geotech. J. 56, 187–197. <https://doi.org/10.1139/cgj-2017-0425>.
- Li, W., Deng, L., 2019. Axial load tests and numerical modeling of single-helix piles in cohesive and cohesionless soils. Acta Geotech. 14, 461–475. <https://doi.org/10.1007/s11440-018-0669-y>.
- Likitlersuang, S., Surarak, C., Wanatowski, D., Oh, E., Balasubramanian, A., 2013. Finite element analysis of a deep excavation: A case study from the Bangkok MRT. Soils Found. 53, 756–773. <https://doi.org/10.1016/j.sandf.2013.08.013>.
- Livneh, B., El Naggar, M.H., 2008. Axial testing and numerical modeling of square shaft helical piles under compressive and tensile loading. Can. Geotech. J. 45, 1142–1155. <https://doi.org/10.1139/T08-044>.
- Malik, A.A., Kuwano, J., 2020. Single helix screw pile behavior under compressive loading/unloading cycles in dense sand. Geotech. Geol. Eng. 38, 5565–5575. <https://doi.org/10.1007/s10706-020-01385-4>.
- Malik, A.A., Kuwano, J., Tachibana, S., Maejima, T., 2019. Effect of helix bending deflection on load settlement behaviour of screw pile. Acta Geotech. 14, 1527–1543. <https://doi.org/10.1007/s11440-019-00778-x>.

- Matsumoto, T., Nemoto, H., Mikami, H., Yaegashi, K., Arai, T., Kitiyodom, P., 2010. Load tests of piled raft models with different pile head connection conditions and their analyses. *Soils Found.* 50, 63–81. <https://doi.org/10.3208/sandf.50.63>.
- Mittal, S., Ganjoo, B., Shekhar, S., 2010. Static equilibrium of screw anchor pile under lateral load in sands. *Geotech. Geol. Eng.* 28, 717–725. <https://doi.org/10.1007/s10706-010-9342-4>.
- Mittal, S., Mukherjee, S., 2015. Behaviour of group of helical screw anchors under compressive loads. *Geotech. Geol. Eng.* 33, 575–592. <https://doi.org/10.1007/s10706-015-9841-4>.
- Mohajerani, A., Bosnjak, D., Bromwich, D., 2016. Analysis and design methods of screw piles: A review. *Soils Found.* 56, 115–128. <https://doi.org/10.1016/j.sandf.2016.01.009>.
- Mori, G., 2003. Development of the screw steel pipe pile with toe wing (Tsubasa Pile), in: *Proceedings of the 4th International Geotechnical Seminar on Deep Foundations on Bored and Auger Piles*. Millpress, Ghent, Belgium, pp. 171–176. [https://doi.org/ISBN 90-77017-76-3](https://doi.org/ISBN%2090-77017-76-3)
- Nagai, H., Tsuchiya, T., Shimada, M., 2018. Influence of installation method on performance of screwed pile and evaluation of pulling resistance. *Soils Found.* 58, 355–369. <https://doi.org/10.1016/j.sandf.2018.02.006>.
- Nakai, T., Hinokio, M., 2004. A simple elastoplastic model for normally and over consolidated soils with unified material parameters. *Soils Found.* 44, 53–70.
- Potyondy, J.G., 1961. *Skin Friction between Various Soils and Construction Materials*. *Geotechnique* 11, 339–353.
- Robinsky, E.I., Morrison, C.F., 1964. Sand Displacement and Compaction around Model Friction Piles. *Can. Geotech. J.* 1, 81–93. <https://doi.org/10.1139/t64-002>.
- Sakr, M., 2014. Relationship between installation torque and axial capacities of helical piles in cohesionless soils. *Can. Geotech. J.* 52, 747–759. <https://doi.org/10.2135/cropsci2016.05.0343>.
- Sakr, M., 2011. Installation and performance characteristics of high capacity helical piles in cohesionless soils. *Deep Foundation Institute Journal. DFI J.* 5, 39–57.
- Sakr, M., 2009. Performance of helical piles in oil sand. *Can. Geotech. J.* 46, 1046–1061. <https://doi.org/10.1139/T09-044>.
- Schanz, T., Vermeer, P.A., Bonnier, P.G., 1999. The hardening soil model: Formulation and verification. *Beyond 2000 Comput. Geotech. Ten Years PLAXIS Int. Proc. Int. Symp. Amsterdam, March 1999*. 281–296. <https://doi.org/10.1201/9781315138206-27>
- Suryasentana, S.K., Lehane, B.M., 2014. Numerical derivation of CPT-based p-y curves for piles in sand. *Geotechnique* 64, 186–194. <https://doi.org/10.1680/geot.13.P.026>.
- Tsuha, C. de H.C., Aoki, N., 2010. Relationship between installation torque and uplift capacity of deep helical piles in sand. *Can. Geotech. J.* 47, 635–647. <https://doi.org/10.1139/T09-128>
- Unsever, Y.S., Matsumoto, T., Özkan, M.Y., 2015. Numerical analyses of load tests on model foundations in dry sand. *Comput. Geotech.* 63, 255–266. <https://doi.org/10.1016/j.compgeo.2014.10.005>.
- Usesugi, M., Kishida, H., 1986. Frictional Resistance at Yield between Dry Sand and Mild Steel. *Soils Found.* 26, 139–149.
- Winter, R., Levine, H.S., 1978. Nonlinear behavior of circular plates with work hardening. *Exp. Mech.* 18, 281–291. <https://doi.org/10.1007/bf02324158>.
- Yamamoto, K., Kusuda, K., 2001. Failure mechanisms and bearing capacities of reinforced foundations. *Geotext. Geomembranes* 19, 127–162. [https://doi.org/10.1016/S0266-1144\(01\)00003-6](https://doi.org/10.1016/S0266-1144(01)00003-6).
- Yang, J., 2006. Influence zone for end bearing of piles in sand. *J. Geotech. Geoenviron. Eng.* 132, 1229–1237. [https://doi.org/10.1061/\(ASCE\)1090-0241\(2006\)132:9\(1229\)](https://doi.org/10.1061/(ASCE)1090-0241(2006)132:9(1229)).
- Yttrup, P.J., Abramsson, G., 2003. Ultimate strength of steel screw piles in sand. *Aust. Geomech. J.* 38, 17–27.